A support-operator method for 3-D rupture dynamics

Geoffrey P. Ely,[1,2] Steven M. Day[3] and Jean-Bernard Minster[1]

[1]*Scripps Institution of Oceanography, University of California, San Diego,* 9500 *Gilman Drive, La Jolla,* CA 92093-0225, *USA.*
E-mail: gely@usc.edu
[2]*Department of Earth Sciences, University of Southern California,* 3651 *Trousdale Parkway, Los Angeles,* CA 90089-0740, *USA*
[3]*Department of Geological Sciences, San Diego State University,* 5500 *Campanile Drive, San Diego,* CA 92182-1020, *USA*

SUMMARY
We present a numerical method to simulate spontaneous shear crack propagation within a heterogeneous, 3-D, viscoelastic medium. Wave motions are computed on a logically rectangular hexahedral mesh, using the generalized finite-difference method of Support Operators (SOM). This approach enables modelling of non-planar surfaces and non-planar fault ruptures. Our implementation, the Support Operator Rupture Dynamics (SORD) code, is highly scalable, enabling large-scale, multiprocessors calculations. The fault surface is modelled by coupled double nodes, where rupture occurs as dictated by the local stress conditions and a frictional failure law. The method successfully performs test problems developed for the Southern California Earthquake Center (SCEC)/U.S. Geological Survey (USGS) dynamic earthquake rupture code validation exercise, showing good agreement with semi-analytical boundary integral method results. We undertake further dynamic rupture tests to quantify numerical errors introduced by shear deformations to the hexahedral mesh. We generate a family of meshes distorted by simple shearing, in the along-strike direction, up to a maximum of 73°. For SCEC/USGS validation problem number 3, grid-induced errors increase with mesh shear angle, with the logarithm of error approximately proportional to angle over the range tested. At 73°, rms misfits are about 10 per cent for peak slip rate, and 0.5 per cent for both rupture time and total slip, indicating that the method (which, up to now, we have applied mainly to near-vertical strike-slip faulting) is also capable of handling geometries appropriate to low-angle surface-rupturing thrust earthquakes. Additionally, we demonstrate non-planar rupture effects, by modifying the test geometry to include, respectively, cylindrical curvature and sharp kinks.

Key words: Numerical solutions; Earthquake dynamics; Computational seismology; Wave propagation.

1 INTRODUCTION

The simulation of earthquake rupture dynamics on non-planar faults embedded in a 3-D, heterogeneous medium has been addressed by a number of methods. Harris & Day (1999), Magistrale & Day (1999) and Harris *et al.* (2002) used finite-difference methods; Aagaard (1999), Oglesby *et al.* (2000) and Oglesby (2005) used finite-element methods; Festa (2004) used spectral-element methods; Zhang *et al.* (2006), Kase & Day (2006) and Cruz-Atienza *et al.* (2007) used modified finite-difference schemes and Benjemaa *et al.* (2009) used a finite-volume technique. The high spatial sampling necessary to adequately resolve the rupture process presents a substantial computational challenge to most methods. Unstructured meshes with adaptive local refinement is a strategy employed by some. The limitations of adaptive meshing are that grid generation is more cumbersome, and algorithms may be less efficient and more difficult to adapt for parallel computation. A more

'brute force' approach is to densely sample the model everywhere with a mesh of regular structure and to exploit that structure to create highly efficient and parallelizable algorithms. We have adopted the latter approach, using the method of support operators (SOM), a generalized finite-difference method introduced by Samarskii *et al.* (1981, 1982) and Shashkov (1996). The SOM was applied to 3-D elastic wave propagation by Ely *et al.* (2008), and we extend that application here to including modelling of spontaneous rupture.

This paper begins by first reviewing the formulation for the wave propagation equations and the spontaneous rupture boundary condition. We then lay out the discretization scheme and algorithm for computing numerical solutions. Next, we verify the method against semi-analytical solutions computed with the boundary integral method. We then quantify errors induced due to deformation of the mesh by simple shearing. Finally, we study the effects of curved and kinked fault geometry on spontaneous rupture.

2 THEORETICAL FORMULATION

The faulting model is embedded within a 3-D, heterogeneous, viscoelastic solid. The linearized equations of motion for the medium are

$$\mathbf{g} = \nabla(\mathbf{u} + \gamma\mathbf{v}), \tag{1}$$

$$\boldsymbol{\sigma} = \lambda\,\text{trace}(\mathbf{g})\mathbf{I} + \mu(\mathbf{g} + \mathbf{g}^{\mathrm{T}}), \tag{2}$$

$$\mathbf{a} = \frac{1}{\rho}\,\nabla \cdot \boldsymbol{\sigma}, \tag{3}$$

$$\dot{\mathbf{v}} = \mathbf{a}, \tag{4}$$

$$\dot{\mathbf{u}} = \mathbf{v}, \tag{5}$$

where $\boldsymbol{\sigma}$ is the stress tensor, $\mathbf{u}$ and $\mathbf{v}$ are displacement and velocity vectors, ρ is density, λ and μ are elastic moduli and γ is viscosity. All variables are functions of position $\mathbf{x}$, whereas $\boldsymbol{\sigma}$, $\mathbf{u}$, and $\mathbf{v}$ are time-dependent as well.

Two types of boundary conditions are employed over the external surface of the model: a traction-free surface condition ($\boldsymbol{\sigma} \cdot \hat{\mathbf{n}} = 0$) and a non-reflective absorbing boundary layer. The absorbing layer condition is an adaption of the perfectly matched layer (PML) method, introduced by Berenger (1994, 1996), and used for dynamic rupture simulation by Ma & Liu (2006). The free surface and PML implementations are detailed by Ely *et al.* (2008).

Following Day *et al.* (2005), faulting is modelled as an internal surface Σ, across which discontinuity of displacement may occur. The unit normal $\hat{\mathbf{n}}(\mathbf{x})$ points from the Σ_- side to the Σ_+ side of the surface Σ. The limiting values of displacement $\mathbf{u}_-$ and $\mathbf{u}_+$, at the surface Σ are

$$\mathbf{u}_{\pm}(\mathbf{x}, t) = \lim_{\epsilon \to 0} \mathbf{u}(\mathbf{x} \pm \epsilon\hat{\mathbf{n}}(\mathbf{x}), t). \tag{6}$$

The two sides are permitted to separate but not to interpenetrate; so, the relative normal displacement must be positive,

$$\hat{\mathbf{n}} \cdot (\mathbf{u}_+ - \mathbf{u}_-) \geq 0. \tag{7}$$

The tangential discontinuity of displacement is denoted 'slip' and given by

$$\mathbf{s} = (\mathbf{I} - \hat{\mathbf{n}}\hat{\mathbf{n}}) \cdot (\mathbf{u}_+ - \mathbf{u}_-), \tag{8}$$

where $\mathbf{I}$ is the identity tensor and $\hat{\mathbf{n}}\hat{\mathbf{n}}$ is the outer product of the unit normal with itself. Stress is continuous across Σ and, when dotted with the unit normal, is resolved onto Σ to give traction

$$\boldsymbol{\tau} = \boldsymbol{\sigma} \cdot \hat{\mathbf{n}}. \tag{9}$$

Traction is the surface density of force acting on $^-\Sigma$ due to $^+\Sigma$. The shear component of traction is

$$\boldsymbol{\tau}_{\mathrm{s}} = (\mathbf{I} - \hat{\mathbf{n}}\hat{\mathbf{n}}) \cdot \boldsymbol{\tau}. \tag{10}$$

The rupture boundary condition is formulated by specifying a frictional strength τ_{c} that is a bound on the magnitude of shear traction

$$|\boldsymbol{\tau}_{\mathrm{s}}| \leq \tau_{\mathrm{c}}. \tag{11}$$

When shear traction is less than the frictional strength, slip does not occur, and Σ is invisible to elastic waves. Slip only occurs when shear traction reaches the level of the frictional strength. Slip velocity opposes the direction of the shear traction according to the relation

$$\tau_{\mathrm{c}}\dot{\mathbf{s}} = |\dot{\mathbf{s}}|\boldsymbol{\tau}_{\mathrm{s}}. \tag{12}$$

This specifies that direction of slip velocity is antiparallel to traction, since the relative slip velocity of $^-\Sigma$ has the opposite sign of $\dot{\mathbf{s}}$.

For the friction law, we use the slip-weakening model (Andrews 1976) that evolves as a function of the slip path length. The path length is found by the integral

$$\ell = \int_0^t |\dot{\mathbf{s}}|\,\mathrm{dt}. \tag{13}$$

The frictional strength is equal to the product of the normal traction and a coefficient of friction,

$$\tau_{\mathrm{c}} = -\tau_{\mathrm{n}}\mu_{\mathrm{f}}(\ell). \tag{14}$$

$$\tau_{\mathrm{n}} = \hat{\mathbf{n}} \cdot \boldsymbol{\sigma} \cdot \hat{\mathbf{n}}, \tag{15}$$

and the coefficient of friction is a function of the slip path length,

$$\mu_{\mathrm{f}}(\ell) = \begin{cases} \mu_{\mathrm{s}} - (\mu_{\mathrm{s}} - \mu_{\mathrm{d}})\ell/d_0 & \ell \leq d_0 \\ \mu_{\mathrm{d}} & \ell > d_0, \end{cases} \tag{16}$$

where μ_{s} and μ_{d} are coefficients of static and dynamic friction, respectively, and d_0 is the critical slip-weakening distance. Generally, the fault is under compression, though dynamic tensional forces may develop under certain conditions. It is assumed that the fault has zero tensional strength and will open in such a case and behave as a free surface. Therefore, the normal stress must always be less than or equal to zero at the fault surface, and the sign of τ_{c} in (14) must always be positive. This model accounts for potentially repeated episodes of rupture initiation and subsequent arrest of sliding, as well as repeated episodes of fault opening, and subsequent fault closing. The methodology can also accommodate more complex friction laws (such as those based on rate- and state-dependent formulations), where there is stationary contact only at zero shear traction, in which case inequality (11) becomes an equality and the distinction between τ and τ_{c} disappears.

Traction is referenced to an initial state $\boldsymbol{\tau}^0$. This can either be resolved from an initial stress field $\boldsymbol{\sigma}^0$, or specified directly in terms of a local coordinate system on the fault, such as the strike and dip coordinate system traditionally used for earthquake problems (Fig. 1). The former is useful for specifying tractions that result, for example, from a regional tectonic load. The latter is most natural when initial traction is determined by local frictional conditions on the fault. In general, they can be combined as

$$\boldsymbol{\tau}^0 = \boldsymbol{\sigma}^0 \cdot \hat{\mathbf{n}} + \tau_n^0\hat{\mathbf{n}} + \tau_{s_1}^0\hat{\mathbf{s}}_1 + \tau_{s_2}^0\hat{\mathbf{s}}_2, \tag{17}$$

where $\hat{\mathbf{s}}_1$ is the strike unit normal and $\hat{\mathbf{s}}_2$ is the dip unit normal. The strike and dip normals can be defined in terms of a downward pointing unit normal $\hat{\mathbf{d}}$ (Fig. 1),

$$\hat{\mathbf{s}}_1 = \hat{\mathbf{n}} \times \hat{\mathbf{d}}, \tag{18}$$

$$\hat{\mathbf{s}}_2 = \hat{\mathbf{s}}_1 \times \hat{\mathbf{n}}. \tag{19}$$

3 NUMERICAL METHOD

Aside from a narrow selection of problems for which analytical solutions have been found, numerical approximations are needed to solve the equations of motion and fault boundary conditions outlined above. Our numerical algorithm discretizes the wave propagation problem using the SOM developed by Ely *et al.* (2008). The scheme is explicit in time and uses a hexahedral structured mesh with rectangular topology. On the mesh we define the space of nodal functions H^N consisting of the hexahedra vertices and the space of
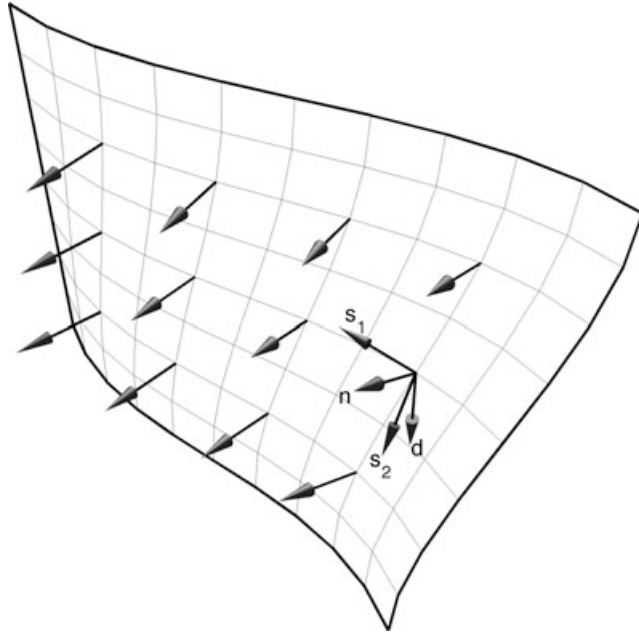
Figure 1. Non-planar fault with surface unit normals. Surface unit normal $\hat{\mathbf{n}}$ and downward unit vector $\hat{\mathbf{d}}$ define the local strike and dip coordinate system $(\hat{\mathbf{s}}_1, \hat{\mathbf{s}}_2, \hat{\mathbf{n}})$.

cell functions H^C consisting of the hexahedra volumes. Discrete variables are defined on the mesh with the same names as their corresponding continuous variables. On the nodes, we have $(\rho, \gamma, \beta, \mathbf{x}, \mathbf{u}, \mathbf{v}, \mathbf{a}, \mathbf{g}) \in H^N$, and on the cells, we have $(\lambda, \mu, \mathcal{Y}, \boldsymbol{\sigma}) \in H^C$. The additional variables, hourglass viscosity β and hourglass stiffness $\mathcal{Y}$, are used for numerical stabilization. Such a discretization gives a partially staggered spatial stencil within the hexahedral mesh, separating the kinematic variables $\mathbf{u}$, $\mathbf{v}$ and $\mathbf{a}$ from the stress tensor $\boldsymbol{\sigma}$.

Spatial derivatives are approximated with the discrete vector difference operators $\mathbf{D}$ and $\mathcal{D}$ (analogous to the ∇ operator of continuous space), which act over the function spaces as follows:

$$\mathbf{D} : H^N \to H^C \quad \text{and} \quad \mathcal{D} : H^C \to H^N. \tag{20}$$

With second-order accurate $\mathbf{D}$ and $\mathcal{D}$ operators, non-uniform stress modes may give rise to numerical instabilities. For hexahedra, there are four non-uniform modes per component of motion, and they are corrected for by four-vector hourglass operators

$$\mathbf{Q} : H^N \to H^C \quad \text{and} \quad \mathcal{Q} : H^C \to H^N. \tag{21}$$

Time is discretized with constant spacing Δt, and time derivatives are approximated with second-order centred differences. The equations of motion (1)–(5) are discretized with time index indicated by a superscript (spatial indices omitted for clarity):

$$\mathbf{g}^n = \mathbf{D}(\mathbf{u}^n + \gamma \mathbf{v}^{n-1/2}), \tag{22}$$

$$\boldsymbol{\sigma}^n = \Lambda \, \mathrm{trace}(\mathbf{g}^n)\mathbf{I} + M(\mathbf{g}^n + (\mathbf{g}^T)^n), \tag{23}$$

$$\mathbf{a}^n = R \, \mathcal{D} \cdot \boldsymbol{\sigma}^n - \mathcal{Q} \cdot \mathcal{Y} \mathbf{Q}(\mathbf{u}^n + \beta \mathbf{v}^{n-1/2}), \tag{24}$$

$$\mathbf{v}^{n+1/2} = \mathbf{v}^{n-1/2} + \Delta t \, \mathbf{a}^n, \tag{25}$$

$$\mathbf{u}^{n+1} = \mathbf{u}^n + \Delta t \, \mathbf{v}^{n+1/2}. \tag{26}$$

The elastic state is stored and updated in $\mathbf{v}^{n+1/2}$ and $\mathbf{u}^{n+1}$, whereas $\mathbf{g}^n$, $\boldsymbol{\sigma}^n$ and $\mathbf{a}^n$ are held temporarily. The discretization is staggered in time with velocity $\mathbf{v}^{n+1/2}$ separated from other variables by $\Delta t/2$.

The material variables incorporate the hexahedral cell volumes V^C, and the node volumes V^N (computed as the mean V^C of the eight cells incorporating each node):

$$\Lambda = \frac{\lambda}{V^C}, \tag{27}$$

$$M = \frac{\mu}{V^C}, \tag{28}$$

$$R = \frac{1}{\rho V^N}. \tag{29}$$

Detailed derivations of difference operators, hourglass corrections and external boundary conditions are provided in Ely *et al.* (2008).

For the fault boundary condition, we use a double-node technique described by Andrews (1999) and Day *et al.* (2005). Here the method is generalized for non-planar surfaces and incorporates the scheme of Day *et al.* to allow for fault opening. The double nodes are constructed by inserting a layer of zero-thickness cells along the fault surface, in which all of the cell valued functions $(\Lambda, M, \mathcal{Y}, \boldsymbol{\sigma})$ are zero. This has the effect of dividing the problem domain into two uncoupled regions, and for the nodal functions, this condition places two sets of colocated values at each fault surface point. Eq. (24) then gives the acceleration for a frictionless free surface at the double nodes. Coupling of the double nodes takes place by applying traction to the frictionless acceleration, to find modified acceleration

$$\tilde{\mathbf{a}}^n_\pm = \mathbf{a}^n_\pm \pm A R_\pm (\boldsymbol{\tau} - \boldsymbol{\tau}^0), \tag{30}$$

where A is the nodal area, the portion of the fault surface area associated with each node. The nodal area is the magnitude of the surface area normal vector as detailed in Appendix A. Similarly, modified velocity is given by

$$\tilde{\mathbf{v}}^{n+1/2}_\pm = \mathbf{v}^{n-1/2}_\pm + \Delta t \, \tilde{\mathbf{a}}^n_\pm, \tag{31}$$

and modified displacement by

$$\tilde{\mathbf{u}}^{n+1}_\pm = \mathbf{u}^n_\pm + \Delta t \, \tilde{\mathbf{v}}^{n+1/2}_\pm. \tag{32}$$

Traction is constructed according to the fault boundary condition eqs (7), (11), (12) and (14). Substituting (31) and (30) into an equation for zero relative modified velocity

$$\tilde{\mathbf{v}}^{n+1/2}_+ - \tilde{\mathbf{v}}^{n+1/2}_- = 0 \tag{33}$$

leads to a trial traction that is the value of traction required for zero relative velocity between the double nodes at time step $n + 1/2$,

$$\tilde{\boldsymbol{\tau}} = \boldsymbol{\tau}^0 + \frac{(\mathbf{v}^{n-1/2}_+ - \mathbf{v}^{n-1/2}_-) + \Delta t \, (\mathbf{a}^n_+ - \mathbf{a}^n_-)}{\Delta t \, A(R_+ + R_-)}. \tag{34}$$

The trial traction, if applied, would lock the current relative locations of the nodes. The tangential contribution to the trial traction is

$$\tilde{\boldsymbol{\tau}}_s = (\mathbf{I} - \hat{\mathbf{n}}\hat{\mathbf{n}}) \cdot \tilde{\boldsymbol{\tau}}. \tag{35}$$

We also calculate a trial value of normal traction required for zero relative normal displacement,

$$\tilde{\tau}_n = \hat{\mathbf{n}} \cdot \left[\tilde{\boldsymbol{\tau}} + \frac{\mathbf{u}^n_+ - \mathbf{u}^n_-}{\Delta t^2 A(R_+ + R_-)} \right]. \tag{36}$$

Table 1. TPV3 model parameters.

Material parameters		
ρ	Density	2670 kg m^{-3}
V_P	P-wave speed	6000 m s^{-1}
V_S	S-wave speed	3464 m s^{-1}
γ	Viscosity	0.02
$\mathcal{Y}$	Hourglass stiffness	1.0
β	Hourglass viscosity	2.0

Fault parameters		Nucleation	Elsewhere
τ_n	Initial normal traction (MPa)	-120	-120
τ_{s1}	Initial shear traction (MPa)	81.6	70.0
μ_s	Coefficient of static friction	0.677	0.677
μ_d	Coefficient of dynamic friction	0.525	0.525
d_0	Slip-weakening distance (m)	0.4	0.4

This traction, if applied, would ensure zero separation of the double nodes, in the fault normal direction. We then apply the condition that normal traction cannot be tensional,

$$\tau_n = \begin{cases} 0, & \tilde{\tau}_n \geq 0 \\ \tilde{\tau}_n, & \tilde{\tau}_n < 0, \end{cases} \tag{37}$$

and the condition that shear traction is bound by the frictional strength

$$\tau_s = \begin{cases} \tau_c, & |\tilde{\boldsymbol{\tau}}_s| \geq \tau_c \\ |\tilde{\boldsymbol{\tau}}_s|, & |\tilde{\boldsymbol{\tau}}_s| < \tau_c. \end{cases} \tag{38}$$

Finally, the total traction on the fault can be assembled,

$$\boldsymbol{\tau} = \tau_n \hat{\mathbf{n}} + \tau_s \frac{\tilde{\boldsymbol{\tau}}_s}{|\tilde{\boldsymbol{\tau}}_s|}, \tag{39}$$

and then the modified nodal accelerations (30) are used to update the nodal velocities by eq. (25).

4 NUMERICAL TESTS

To verify the numerical accuracy of our method, we use one of a series of test problems developed for the dynamic earthquake rupture code validation exercise organized by the Southern California Earthquake Center (SCEC) and the U.S. Geological Survey (USGS) (Harris & Archuleta 2004; Harris *et al.* 2009). For test problem number 3 (TPV3), Day *et al.* (2005) computed both boundary-integral (BI) and finite-difference (FD) solutions to help establish mutual verification of the two methods. We preform a similar analysis here and use the BI solutions from Day *et al.* as a basis to compare TPV3 solutions computed with our SOM method.

TPV3 consists of a finite planar fault within an infinite elastic isotropic medium. The material and fault parameters for TPV3 are given in Table 1. Rupture occurs on a 30×15 km fault (diagrammed in Fig. 2) that is stressed parallel to the x axis. Rupture is nucleated by a 3×3 km patch in which shear traction is higher than the initial static frictional strength $\tau_c(\ell = 0)$. Rupture spreads spontaneously out from the nucleation patch, producing a mixed-mode rupture that reduces to pure mode II along the x axis and pure mode III along the y axis.

Accurate numerical solutions for rupture dynamics problems require sufficient resolution of the cohesive zone. For slip-weakening friction, the cohesive zone is the portion of the fault that has begun slipping but not yet reached its dynamic friction level. Day *et al.* (2005) found that with a mesh resolution of 50 m (which we use for the SOM models), the cohesive zone is sampled with a least 6.5 nodes for TPV3, and that this is sufficient for accurate solutions (e.g. less than 1 per cent error in rupture time) for their method. Their method is equivalent to SOM in the rectangular case; so, those results are informative for SOM as well. The resolution requirement for BI is lower; so, we are able to use the coarser 100 m grid BI solution from Day *et al.*

We preform three SOM calculations, one with a rectangular mesh of node spacing $\Delta x = 50$ m and two more with meshes distorted by simple shearing. The first sheared mesh, pictured in Fig. 2, is constructed from the rectangular mesh by applying the coordinate mapping

$$\begin{bmatrix} X'_{jkl} \\ Y'_{jkl} \\ Z'_{jkl} \end{bmatrix} = \begin{bmatrix} X_{jkl} \\ Y_{jkl} \\ Z_{jkl} \end{bmatrix} + \begin{bmatrix} 0 & 1 & 1 \\ 0 & 0 & 0 \\ 0 & 0 & 0 \end{bmatrix} \begin{bmatrix} X_{jkl} \\ Y_{jkl} \\ -|Z_{jkl}| \end{bmatrix}, \tag{40}$$

where (X, Y, Z) are coordinates of the rectangular mesh and (X', Y', Z') are coordinates of the sheared mesh. We call this mesh 'S23'. The name is derived from positions of the non-zero coefficient in the transformation matrix (second and third positions, where elements
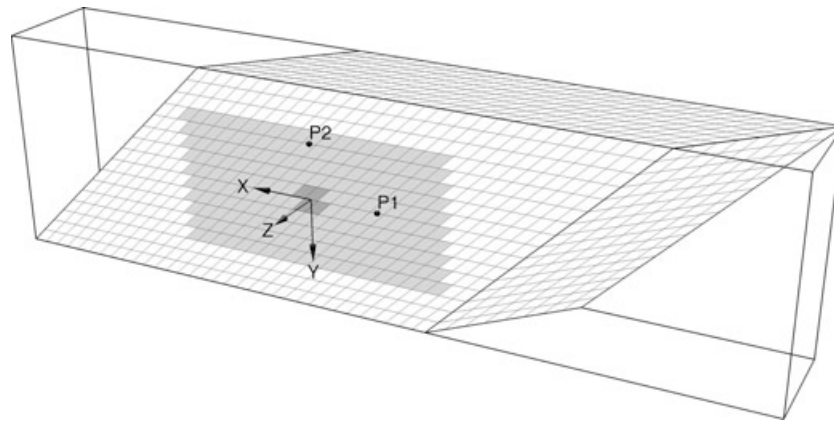

Figure 2. Schematic diagram of the model configuration for sheared mesh S23. The near-fault block (a mirror image of the far block) is removed to allow viewing of the fault surface. Fault surface elements lying within the 30×15 km slipping portion of the fault are shaded grey. Elements in the 3×3 km nucleation patch are shaded dark grey. Slip is right-lateral, with mode II rupture along the x axis and mode III rupture along the y axis. Observation points are located at P1 and P2.

are ordered with column index most rapidly varying). The second sheared mesh, named 'S26', is constructed from the mapping

$$\begin{bmatrix} X'_{jkl} \\ Y'_{jkl} \\ Z'_{jkl} \end{bmatrix} = \begin{bmatrix} X_{jkl} \\ Y_{jkl} \\ Z_{jkl} \end{bmatrix} + \begin{bmatrix} 0 & 1 & 0 \\ 0 & 0 & 1 \\ 0 & 0 & 0 \end{bmatrix} \begin{bmatrix} X_{jkl} \\ Y_{jkl} \\ -|Z_{jkl}| \end{bmatrix}. \qquad (41)$$

Both mappings produce mirror symmetry across the fault plane, 45° shearing of the fault surface and a maximum of 54.7° of shearing in the volume. However, the shapes of the elements are quite different between the two meshes.

To assess the level of agreement between BI and SOM solutions, we first compare the rupture arrival time (defined as the time when slip velocity surpasses 1 mm s^{-1}) over the fault plane. During the early stages of rupture, the rupture arrival times agree closely among BI and SOM solutions (Fig. 3). At later times, the rectangular SOM solution falls behind BI by as much as 0.022 s. The rms difference (averaged over the fault plane) is 0.009 s or about 0.24 per cent of the average rupture time of 3.56 s. Rupture velocities on the sheared meshes are faster in the direction corresponding to
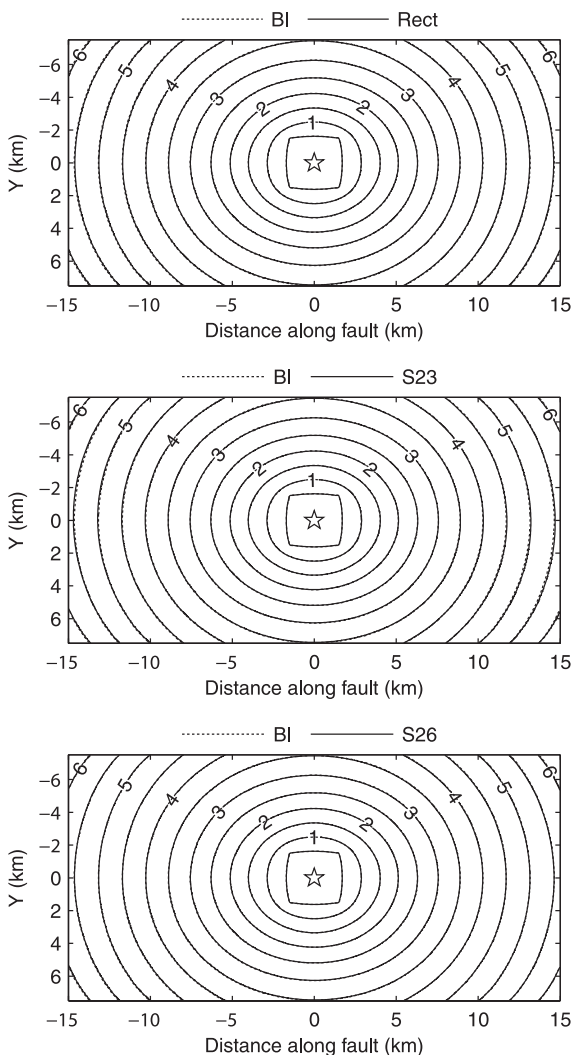
the long axis of the sheared elements, matching BI for S26 and slightly exceeding BI for mesh S23. In the direction of the short axis of the elements, rupture velocities are similar to the rectangular case—slightly slower than BI. The maximum and rms difference are 0.034 s and 0.010 s for mesh S23, and 0.021 s and 0.006 s for mesh S26.

Fig. 4 compares unfiltered times histories of shear traction, slip rate and slip at a point P1, 7.5 km from the origin in the mode II direction. All important features are closely matched, including: waveform shape and amplitude; time of initial rupture at 2.95 s; time of reflected arrival at 6.2 s; time of rupture arrest at 7 s and the time of short rupture reactivation at 8 s. The largest misfit is due to small oscillations in the slip rate. At frequencies lower than the oscillations, the fit is nearly perfect. Fig. 5 shows a similar comparison for point P2, 6 km from the origin in the mode III direction.

Perhaps the most useful mesh deformation for earthquake rupture simulations is shearing in the plane defined by the fault surface normal and the slip vector. Shearing of this orientation does not effect the fault surface elements, and they remain rectangular. Volume element are defected towards or away from the slip vector. This geometry accommodates the case of dip–slip rupture on a dipping fault intersecting the free surface, as well as the case of a vertical strike-slip fault with variable strike. Low-angle thrust faults, in particular, may require drastic element deformations of this type; so, it is important to understand the numerical affects of such deformations. To that end, we ran a series of tests with the mapping
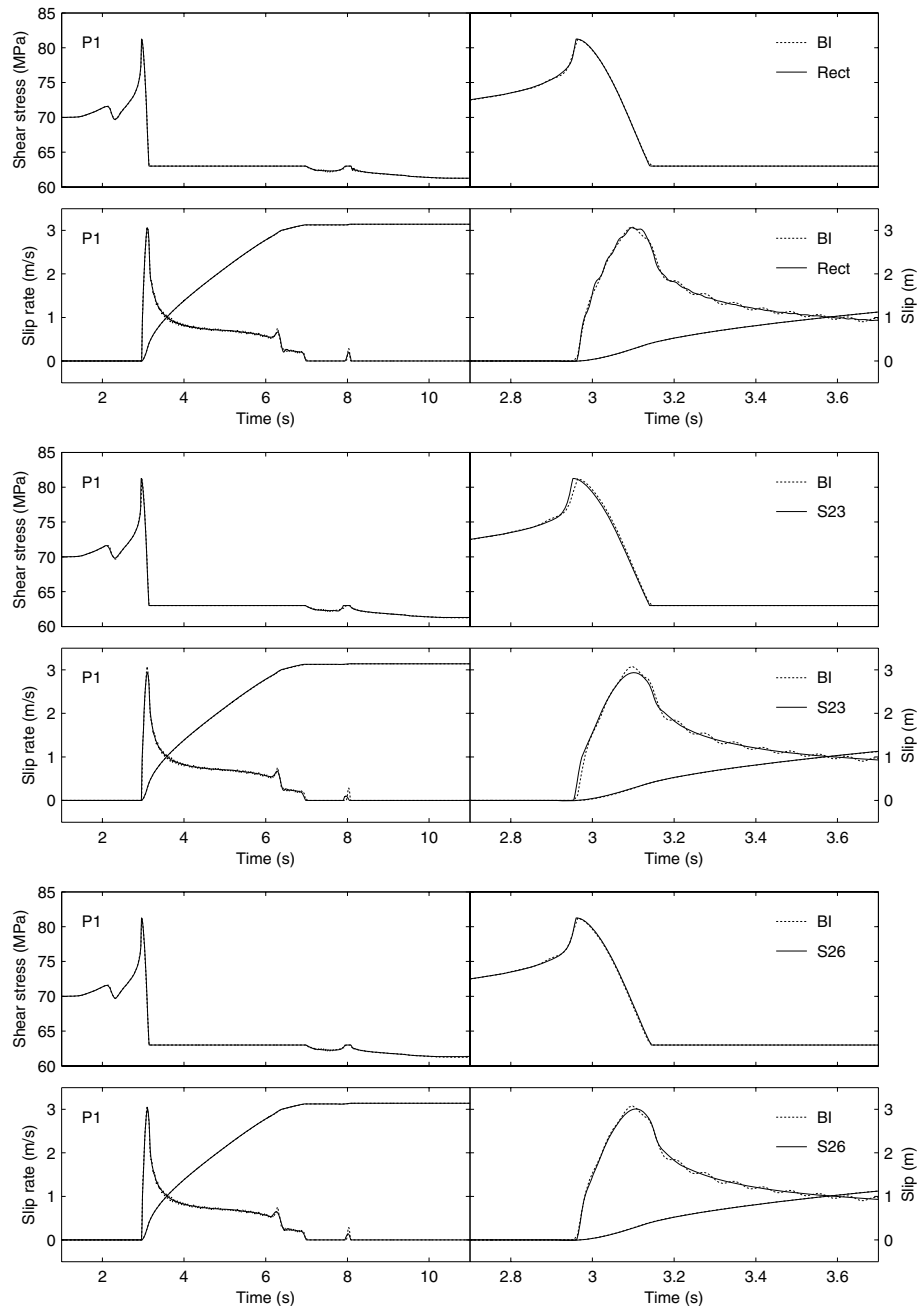
$$\begin{bmatrix} X'_{jkl} \\ Y'_{jkl} \\ Z'_{jkl} \end{bmatrix} = \begin{bmatrix} X_{jkl} \\ Y_{jkl} \\ Z_{jkl} \end{bmatrix} + \begin{bmatrix} 0 & 0 & e_{xz} \\ 0 & 0 & 0 \\ 0 & 0 & 0 \end{bmatrix} \begin{bmatrix} X_{jkl} \\ Y_{jkl} \\ -|Z_{jkl}| \end{bmatrix}, \qquad (42)$$

where e_{xz} is a variable amount of mesh strain. In our naming scheme, this mesh is called 'S3'. Mesh strain was increased to a maximum of 3, in increments of 0.5, resulting in a maximum shear angle of 72.6°.

Numerical errors are assessed by comparing each sheared mesh model to the reference rectangular mesh model. The rms differences in rupture arrival time, slip and peak slip rate are computed for the entire 30 × 15 km slipping portion of the fault. The rms differences increase logarithmically by roughly an order of magnitude over the 26.6°–72.6° range of shearing (Fig. 6). At maximum shear, the difference is 0.5 per cent for rupture time, 0.6 per cent for slip and 10.3 per cent for peak slip rate. These results indicate the method remains highly accurate for applications with modest shearing such as 60° dipping normal faults (30° shear) or vertical strike-slip faults with small changes in strike. Even for low-angle trust faults, with high amounts mesh shear, accuracy is likely acceptable for many applications.

For completeness, we verify convergence of the numerical method with decreasing spatial step size Δx for the rectangular mesh case. As the rectangular case is equivalent to the finite-difference method of Day *et al.* (2005), their analysis directly applies here. We have extended the range of mesh resolutions, reaching $\Delta x = 10$ m at the finest. Fig. 7 illustrates power-law convergence of rms errors in rupture arrival time, slip and peak slip rate. It should noted that convergence of the algorithm with deceasing step size is not proof of correctness, and it is for that reason that the previous comparisons with BI are an essential component of the verification.

The 10 m case consisted of one billion mesh nodes (reduced eight-fold through symmetry in TPV3) computed for 15 000 time

Figure 3. Rupture arrival time contours (s) comparing boundary integral solutions (BI) to SOM solutions for a rectangular mesh and for sheared meshes S23 and S26.

Figure 4. Time histories of shear stress, slip and slip rate for the mode II, in-plane point P1. The right-hand panels are magnified in time to show detail of the rupture arrival.

steps. The simulation required 4 hr to complete using 1024 CPU cores and 250 GB of memory on the Ranger Linux cluster at the Texas Advanced Computing Center. The 50 m case (10 million mesh nodes) can be computed on a modern laptop in about 8 hr.

5 NON-PLANAR FAULTS

Changes in fault direction can play an important role in the nucleation, termination and radiated energy of earthquakes. Non-planar geometry provides a mechanism by which dynamic changes in normal stress (and therefore friction) can occur. Detailed study of non-planar rupture, using a variety of analysis and numerical

methods, include work by Andrews (1989), Tada & Yamashita (1996), Bouchon & Streiff (1997), Aochi *et al.* (2000), Poliakov *et al.* (2002), Duan & Oglesby (2005), Kase & Day (2006), Cruz-Atienza *et al.* (2007), Benjemaa *et al.* (2007) and Adda-Bedia & Madariaga (2008). Laboratory scale model experiments have also been performed by Rousseau & Rosakis (2003). Here we make simple modifications to TPV3 to demonstrate the effects of fault curvature and sharp fault kinks.

Our test problems modify TPV3 by varying the strike direction, keeping the fault vertical, and keeping the total fault length the same at 30 km (Fig. 8). The first test problem has cylindrical fault geometry of radius $90/\pi$ km, with the ends of the fault rotated 30° relative the nucleation point. The second test problem has a
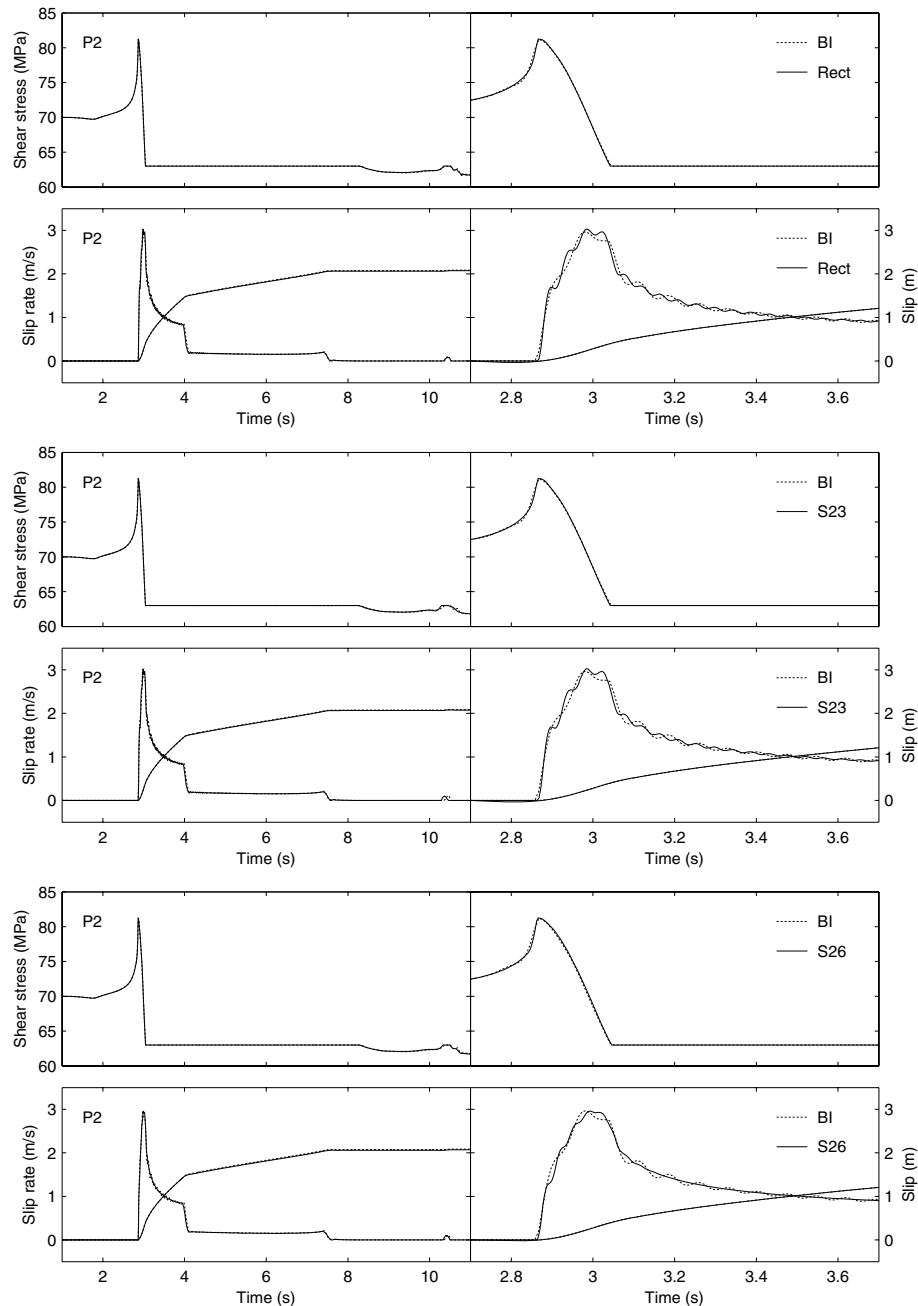
Figure 5. Time histories of shear stress, slip and slip rate for the mode III, anti-plane point P2. The right-hand panels are magnified in time to show detail of the rupture arrival.

kinked geometry consisting of three planar segments with a 30° change in strike 7.5 km from the nucleation point, on either side. The problems are otherwise identical to TPV3. The grids are constructed so that the fault is discretized with square elements having the same 50 m resolution as the rectangular planar model. No elements are sheared more than 30°; so, gauging from the sheared mesh tests, we can expect that rms errors due to mesh shearing will be less than 0.2 per cent for slip, less than 2 per cent for slip rate and less than 0.05 per cent for rupture time.

Typically, non-planar fault studies have set up a uniform external stress field that is resolved onto the fault, resulting in variable traction conditions depending on the fault's local orientation. Here, we

instead rotate the local initial stress field, so that the resolved traction on the fault remains in a fixed orientation relative to the local fault orientation. The magnitudes of initial normal and shear traction are assigned uniform values over the fault surface, regardless of local orientation. The goal is to isolate the effects of non-planar geometry, without introducing heterogeneity in the initial resolved tractions on the fault. This scheme presents a problem for the case of a sharp kink, as it requires a discontinuity of stress at the kink. However, a perfectly sharp discontinuity cannot be represented by discrete equations; so, the sharp kink effectively becomes a curve of radius comparable to the discretization length in the numerical solution.
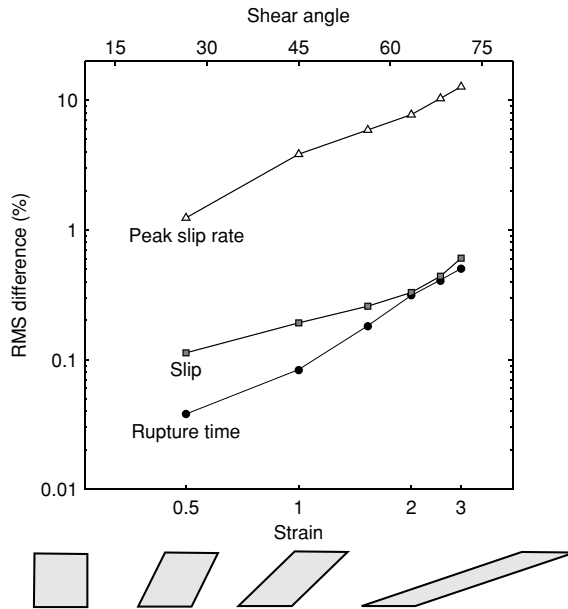
Figure 6. Difference in rupture time, slip and peak slip rate as a function of shear strain applied to the mesh. Values are rms averages over the fault plane, referenced to the rectangular case. The deformed element shapes are depicted along the lower axis.
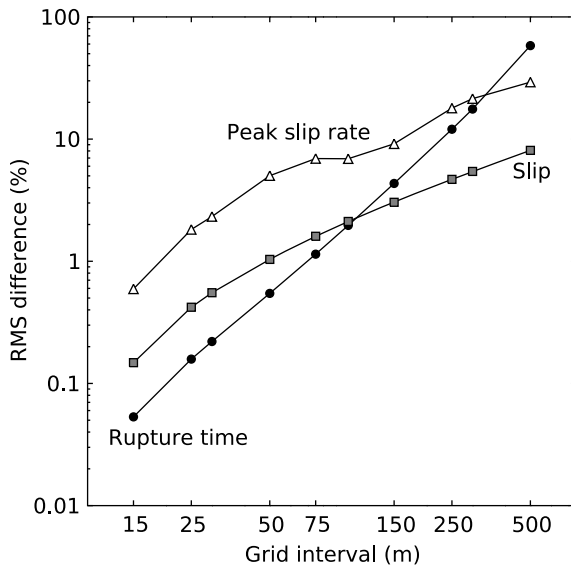
Figure 7. Difference in rupture time, slip and peak slip rate as a function of discretization size Δx. Values are rms averages over the fault plane, referenced to a $\Delta x = 10$ m case.

Symmetry in the planar TVP3 model ensures that normal traction of the fault remains constant at all times. A fundamental difference of the non-planar models is that fault slip induces dynamic changes in normal traction (and frictional strength) at other locations on the fault. In the cylindrical and kinked geometries, right-lateral slip results in decompression (lower strength) in the negative x direction and compression (higher strength) in the positive x direction relative to the axis of the curve or kink. For the cylindrical model, the normal traction change is a gradual, nearly linear function of distance along the fault (Fig. 9). The kinked model develops large stress con-
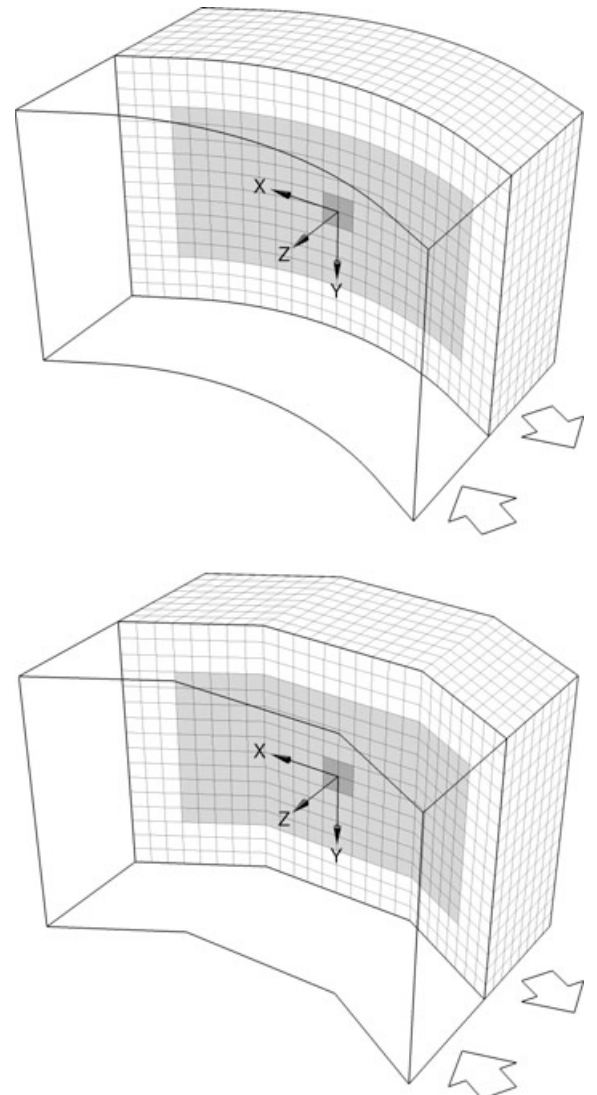

Figure 8. TPV3 modified for cylindrical fault geometry (top panel) and for kinked fault geometry (bottom panel).

centrations at the kinks that rapidly decay with distance from the kink. The stress concentrations have a sign change at the axis of the kink that divides the decompressed side from the compressed side. In both models, the decompressed side has higher rupture velocity (Fig. 10) and higher total slip (Fig. 11).
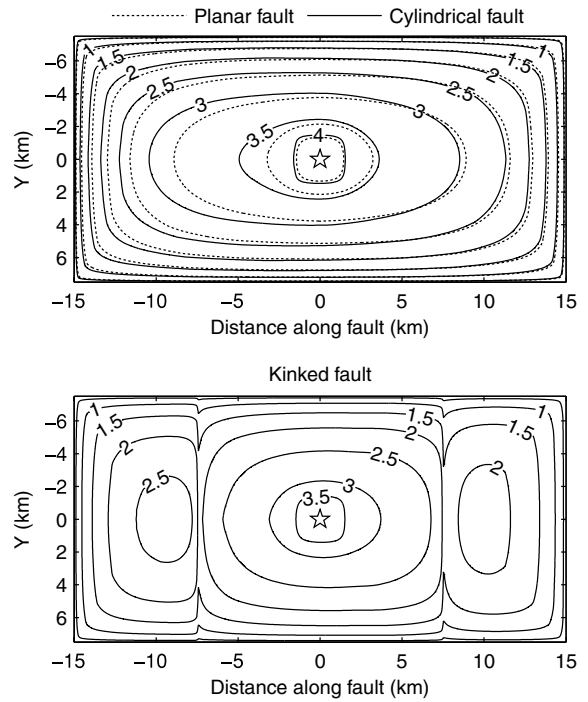
The total moment release for the cylindrical model (34.0×10^{18} N m) is greater than the planar model (33.2×10^{18} N m), and the moment release for the kinked model (27.9×10^{18} N m) is lower than the planar model. The lower moment for the kinked model is due to the partial barriers to slip formed by the kinks, as seen in slip profiles along the in-plane axis (Fig. 12). The kink barrier in the positive x side causes rupture to pause for about 2 s before continuing to the next fault segment. The 2 s pause is clearly visible in a space-times plot of slip acceleration (Fig. 13).

Another effect seen in the space-time plot is the radiation of P and S waves from the fault kicks at the time of their initial rupture. The kinked model in general has a more complicated rupture history compared with the planar and cylindrical models. For the cylindrical model, the space–time plot shows that rupture along the in-plane axis is primarily halted by the P wave reflected from the lateral
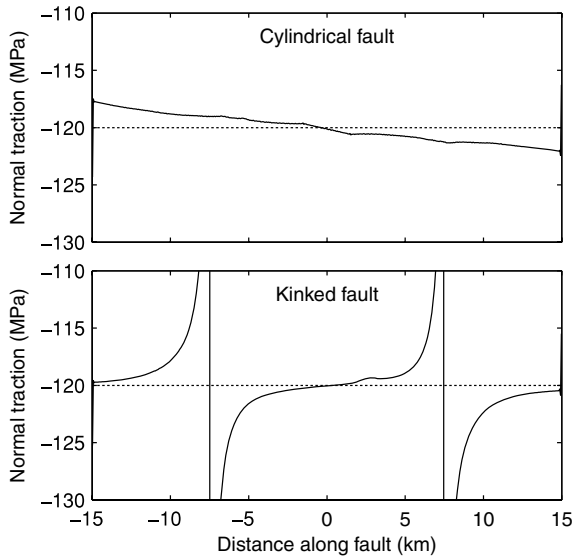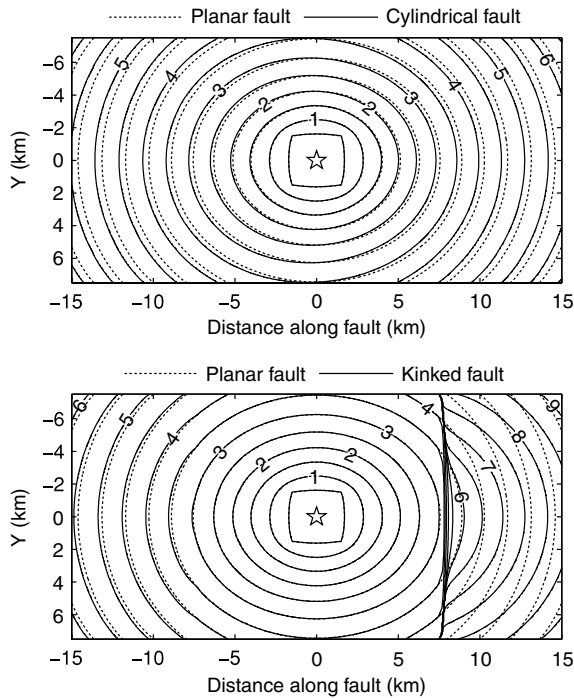
Figure 9. Profile of normal traction along the in-plane (horizontal) axis at time $t = 12$ s for cylindrical and kinked fault models. For both models, during and after rupture, the fault flank along the negative x axis is decompressed, whereas the fault flank along the positive x axis is compressed relative to the initial value of -120 MPa (dotted line). High stress concentrations develop at the kinks.


Figure 10. Rupture arrival time (s) for planar, cylindrical and kinked fault models.

fault boundaries (marked Pi). Toward the edges, rupture is briefly reactivated by laterally reflected *S* waves (Si) or vertically reflected *S* waves (Sa). By contrast, much of the kinked model rupture is halted by the Sa wave. Rupture is reactivated on most of the central segment after rupture begins on the compressed segment following the 2 s pause. This second rupture stage is halted by a Pi wave and in some places briefly reactivated by an Si wave.

Figure 11. Final slip magnitude (m) for planar, cylindrical and kinked fault models.
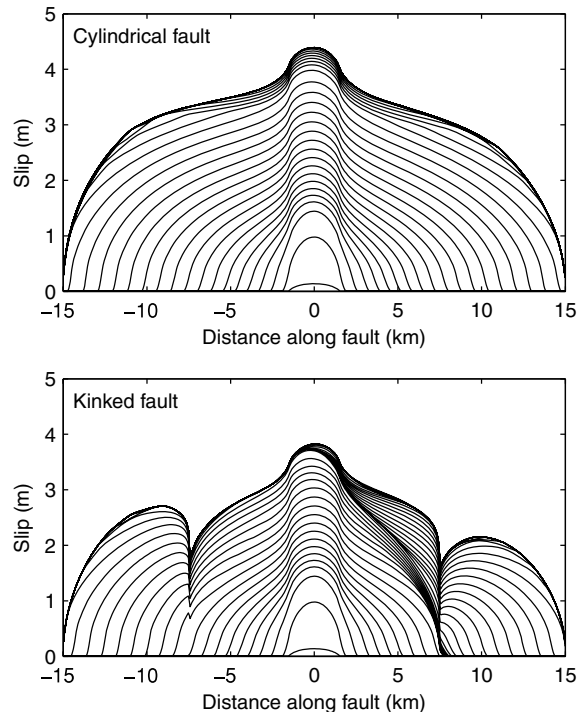
Figure 12. Profile of slip magnitude along the in-plane (horizontal) axis at 0.3 s intervals.

6 CONCLUSION

We have extended the support-operator numerical scheme for 3-D viscoelastic wave propagation, previously developed by Ely *et al.* (2008), to model non-planar spontaneous rupture. We implement a
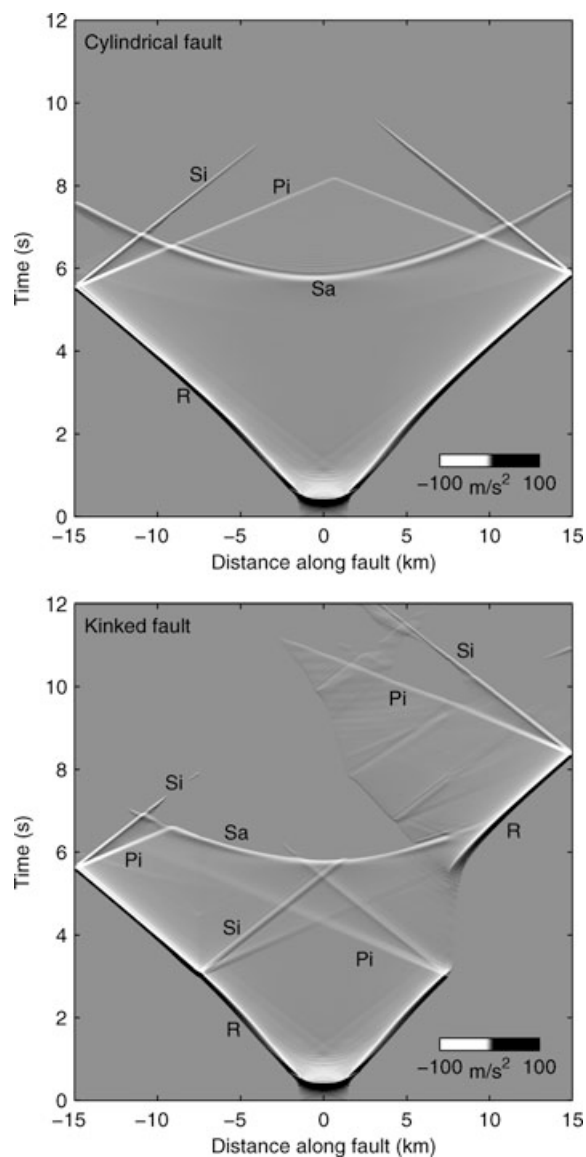
Figure 13. Space–time plots of slip acceleration magnitude along the in-plane (horizontal) axis. R indicates initial rupture. Pi and Si indicate horizontally travelling *P* and *S* waves, reflected by kinks and lateral fault boundaries. Sa indicates vertically travelling *S* waves reflected by the top and bottom fault boundaries.

slip-weakening friction model, and the method is readily adaptable to other types of friction laws. The method is verified against a boundary integral solution for planar rupture problems, using both rectangular meshes and meshes distorted by shearing. The accuracy of the sheared mesh tests indicates that the method is also suitable for modelling low-angle surface rupturing thrust faults. Non-planar rupture effects were demonstrated using a cylindrical fault geometry as well as a planar segmented, or kinked, geometry. The kinked geometry introduces significant rupture complexity relative to planar and cylindrical cases, with the kinks acting as partial barriers to slip that lead to high stress concentrations.

ACKNOWLEDGMENTS

REFERENCES

Aagaard, B.T., 1999. Finite-element simulations of earthquakes, Technical Report EERL-99-03, California Institute of Technology, Earthquake Engineering Research Laboratory, Pasadena, CA.

Adda-Bedia, M. & Madariaga, R., 2008. Seismic radiation from a kink on an antiplane fault, *Bull. seism. Soc. Am.,* **98**(5), 2291–2302.

Andrews, D.J., 1976. Rupture propagation with finite stress in antiplane strain, *J. geophys. Res.,* **81**(B20), 3575–3582.

Andrews, D.J., 1989. Mechanics of fault junctions, *J. geophys. Res.,* **94**(B7), 9389–9397.

Andrews, D.J., 1999. Test of two methods for faulting in finite-difference calculations, *Bull. seism. Soc. Am.,* **89**(4), 931–937.

Aochi, H., Fukuyama, E. & Matsuâura, M., 2000. Spontaneous rupture propagation on a non-planar fault in 3-D elastic medium, *Pure appl. Geophys.,* **157**(11), 2003–2027.

Benjemaa, M., Glinsky-Olivier, N., Cruz-Atienza, V.M., Virieux, J. & Piperno, S., 2007. Dynamic non-planar crack rupture by a finite volume method, *Geophys. J. Int.,* **171**(1), 271–285.

Benjemaa, M., Glinsky-Olivier, N., Cruz-Atienza, V.M. & Virieux, J., 2009. 3D dynamic rupture simulations by a finite volume method, *Geophys. J. Int.,* doi:10.1111/j.1365-246X.2009.04088.x.

Berenger, J.-P., 1994. A perfectly matched layer for the absorption of electromagnetic waves, *J. Comput. Phys.,* **114**(2), 185–200.

Berenger, J.-P., 1996. Three-dimensional perfectly matched layer for the absorption of electromagnetic waves, *J. Comput. Phys.,* **127**(2), 363–379.

Bouchon, M. & Streiff, D., 1997. Propagation of a shear crack on a nonplanar fault: a method of calculation, *Bull. seism. Soc. Am.,* **87**(1), 61–66.

Cruz-Atienza, V.M., Virieux, J. & Aochi, H., 2007. 3D finite-difference dynamic-rupture modelling along non-planar faults, *Geophysics,* **72**(5), SM123–SM137.

Day, S.M., Dalguer, L.A., Lapusta, N. & Liu, Y., 2005. Comparison of finite difference and boundary integral solutions to three-dimensional spontaneous rupture, *J. geophys. Res.*, **110**, B12307.

Duan, B. & Oglesby, D.D., 2005. Multicycle dynamics of nonplanar strike-slip faults, *J. geophys. Res.*, **110**, B03304.

Ely, G.P., Day, S.M. & Minster, J.-B.H., 2008. A support-operator method for visco-elastic wave modeling in 3-D heterogeneous media, *Geophys. J. Int.,* **172**(1), 331–344.

Festa, G., 2004. Fault dynamics with spectral elements and slip imaging by isochone back-projection, *PhD thesis*, Alma Mater Studiorum—Università di Bologna, Bologna.

Harris, R.A. & Archuleta, R.J., 2004. Earthquake rupture dynamics: comparing the numerical simulation methods, *EOS, Trans. Am. geophys. Un.,* **85**(34), 321.

Harris, R.A. & Day, S.M., 1999. Dynamic three-dimensional simulations of earthquakes on en echelon faults, *Geophys. Res. Lett.,* **26**(14), 2089–2092.

Harris, R.A., Dolan, J.F., Hartleb, R. & Day, S.M., 2002. The 1999 Izmit, Turkey, earthquake: a 3D dynamic stress transfer model of intraearthquake triggering, *Bull. seism. Soc. Am.,* **92**(1), 245–255.

Harris, R.A. *et al.*, 2009. The SCEC/USGS dynamic earthquake rupture code validation exercise, *Seism. Res. Lett.,* **80**(1), 119–126.

Kase, Y. & Day, S.M., 2006. Spontaneous rupture processes on a bending fault, *Geophys. Res. Lett.*, **33**, L10302.

Ma, S. & Liu, P., 2006. Modeling of the perfectly matched layer absorbing boundaries and intrinsic attenuation in explicit finite-element methods, *Bull. seism. Soc. Am.,* **96**(5), 1779–1794.

Magistrale, H. & Day, S.M., 1999. Three-dimensional simulations of multisegment thrust fault rupture, *Geophys. Res. Lett.,* **26**(14), 2093–2096.

Oglesby, D.D., 2005. The dynamics of strike-slip step-overs with linking dip-slip faults, *Bull. seism. Soc. Am.,* **95**(5), 1604–1622.

Oglesby, D.D., Archuleta, R.J. & Nielsen, S.B., 2000. The three-dimensional dynamics of dipping faults, *Bull. seism. Soc. Am.,* **90**(3), 616–628.

Poliakov, A.N.B., Dmowska, R. & Rice, J.R., 2002. Dynamic shear rupture interactions with fault bends and off-axis secondary faulting, *J. geophys. Res.,* **107**(B11), 2295.

Rousseau, C.-E. & Rosakis, A.J., 2003. On the influence of fault bends on the growth of sub-Rayleigh and intersonic dynamic shear ruptures, *J. geophys. Res.,* **108**(B9), 2411.

Samarskii, A., Tishkin, V., Favorskii, A. & Shashkov, M., 1981. Operational finite-difference schemes, *Diff. Eqns.,* **17,** 854–862.

Samarskii, A., Tishkin, V., Favorskii, A. & Shashkov, M., 1982. Employment of the reference-operator method in the construction of finite difference analogs of tensor operations, *Diff. Eqns.,* **18,** 881–885.

Shashkov, M., 1996. *Conservative Finite-Difference Methods on General Grids*, CRC Press, Boca Raton, FL.

Tada, T. & Yamashita, T., 1996. The paradox of smooth and abrupt bends in two-dimensional in-plane shear-crack mechanics, *Geophys. J. Int.,* **127**(3), 795–800.

Zhang, W., Iwata, T. & Irikura, K., 2006. Dynamic simulation of a dipping fault using a three-dimensional finite difference method with nonuniform grid spacing, *J. geophys. Res.,* **111,** B05301.

APPENDIX: CALCULATION OF SURFACE NORMALS AND NODAL AREAS

Surface normals and nodal areas are needed for the fault boundary calculations. On a hexahedral mesh, they may be found as follows. Quadratic interpolation of 3×3 stencil of boundary surface nodes with coordinates $\mathbf{X}_{jk}$ is given by

$$\mathbf{x}(\boldsymbol{\xi}) = \sum_{j,k=0}^{2} N_{jk}(\boldsymbol{\xi}) X_{jk}, \tag{A1}$$

where the shape functions $N_{jkl}(\boldsymbol{\xi})$ are formed from Lagrange interpolation polynomials

$$N_{jk}(\boldsymbol{\xi}) = \ell_j^2(\xi)\ell_k^2(\eta). \tag{A2}$$

The Lagrange polynomials of degree 2 are

$$\ell_j^2(\xi) = \prod_{\substack{i=0 \\ i \neq j}}^{2} \frac{\xi - \Xi_i}{\Xi_j - \Xi_i}. \tag{A3}$$

The interpolation maps continuous Cartesian coordinates $\mathbf{x}$ to logical coordinates $\boldsymbol{\xi}$ and discrete nodal coordinates $\mathbf{X}_{jk}$ to logical nodal coordinates Ξ_{jk}. Surface area vectors are given by the Jacobian of the coordinate mapping:

$$d\mathbf{S} = \frac{\partial \mathbf{x}}{\partial \xi} \times \frac{\partial \mathbf{x}}{\partial \eta} = \begin{bmatrix} \left| \begin{matrix} \dfrac{\partial y}{\partial \xi} & \dfrac{\partial z}{\partial \xi} \\ \dfrac{\partial y}{\partial \eta} & \dfrac{\partial z}{\partial \eta} \end{matrix} \right| \\ \left| \begin{matrix} \dfrac{\partial z}{\partial \xi} & \dfrac{\partial x}{\partial \xi} \\ \dfrac{\partial z}{\partial \eta} & \dfrac{\partial x}{\partial \eta} \end{matrix} \right| \\ \left| \begin{matrix} \dfrac{\partial x}{\partial \xi} & \dfrac{\partial y}{\partial \xi} \\ \dfrac{\partial x}{\partial \eta} & \dfrac{\partial y}{\partial \eta} \end{matrix} \right| \end{bmatrix}. \tag{A4}$$

The magnitude of the Jacobian $J = |d\mathbf{S}|$ gives the area associated with each mesh node, and the surface unit normal is $\hat{\mathbf{n}} = d\mathbf{S}/J$. Evaluating (A4) at the central node Ξ_{11} gives the following expressions for the components of $d\mathbf{S}(\Xi_{11})$:

$$\begin{aligned} dS_{11}^x = \frac{1}{12}\big[& Y_{21}(Z_{12} - Z_{10} + Z_{22} - Z_{20}) \\ & + Y_{12}(Z_{01} - Z_{21} + Z_{02} - Z_{22}) \\ & + Y_{01}(Z_{10} - Z_{12} + Z_{00} - Z_{02}) \\ & + Y_{10}(Z_{21} - Z_{01} + Z_{20} - Z_{00}) \\ & + Y_{22}(Z_{12} - Z_{21}) \\ & + Y_{00}(Z_{10} - Z_{01}) \\ & + Y_{02}(Z_{01} - Z_{12}) \\ & + Y_{20}(Z_{21} - Z_{10})\big], \end{aligned} \tag{A5}$$

$$\begin{aligned} dS_{11}^y = \frac{1}{12}\big[& Z_{21}(X_{12} - X_{10} + X_{22} - X_{20}) \\ & + Z_{12}(X_{01} - X_{21} + X_{02} - X_{22}) \\ & + Z_{01}(X_{10} - X_{12} + X_{00} - X_{02}) \\ & + Z_{10}(X_{21} - X_{01} + X_{20} - X_{00}) \\ & + Z_{22}(X_{12} - X_{21}) \\ & + Z_{00}(X_{10} - X_{01}) \\ & + Z_{02}(X_{01} - X_{12}) \\ & + Z_{20}(X_{21} - X_{10})\big], \end{aligned} \tag{A6}$$

$$\begin{aligned} dS_{11}^z = \frac{1}{12}\big[& X_{21}(Y_{12} - Y_{10} + Y_{22} - Y_{20}) \\ & + X_{12}(Y_{01} - Y_{21} + Y_{02} - Y_{22}) \\ & + X_{01}(Y_{10} - Y_{12} + Y_{00} - Y_{02}) \\ & + X_{10}(Y_{21} - Y_{01} + Y_{20} - Y_{00}) \\ & + X_{22}(Y_{12} - Y_{21}) \\ & + X_{00}(Y_{10} - Y_{01}) \\ & + X_{02}(Y_{01} - Y_{12}) \\ & + X_{20}(Y_{21} - Y_{10})\big]. \end{aligned} \tag{A7}$$

Quadratic interpolation cannot be used at the edge and corners nodes of the surface, where the 3×3 stencil would otherwise extend outside of the mesh. In this case, we may instead use linear interpolation in the direction normal to the edge. Fortunately, this does not require constructing separate operators for each special case. It is handled more simply by extending the mesh with ghost nodes, and duplicating the edge node coordinates into the ghost nodes. It can be shown that when the interior operators (A5)–(A7) are applied at edges with such ghost nodes, the equations naturally reduce to the proper linear interpolation equations.